



Cite this: DOI: 10.1039/d1sm00559f

## Red blood cells in low Reynolds number flow: A vorticity-based characterization of shapes in two dimensions†

 Andreu F. Gallen, \*<sup>a</sup> Mario Castro <sup>b</sup> and Aurora Hernandez-Machado <sup>ac</sup>

Studies on the mechanical properties of red blood cells improve the diagnosis of some blood-related diseases. Some existing numerical methods have successfully simulated the coupling between a fluid and red blood cells. This paper introduces an alternative phase-field model formulation of two-dimensional cells that solves the vorticity and stream function that simplifies the numerical implementation. We integrate red blood cell dynamics immersed in a Poiseuille flow and reproduce previously reported morphologies (slippers or parachutes). In the case of flow in a very wide channel, we discover a new metastable shape referred to as 'anti-parachute' that evolves into a horizontal slipper centered on the channel. This sort of metastable morphology may contribute to the dynamical response of the blood.

 Received 16th April 2021,  
 Accepted 21st September 2021

DOI: 10.1039/d1sm00559f

[rsc.li/soft-matter-journal](http://rsc.li/soft-matter-journal)

## 1 Introduction

The mechanical properties of a red blood cell (RBC) has profound implications in the diagnosis of some blood-related diseases.<sup>1–3</sup> The velocity of plasma or the degree of confinement affects the shape and mechanical response of the cells in unexpected ways.<sup>4–6</sup>

Many approaches have exploited the unique ability of computer simulations to understand dynamics *in silico*, ranging from mesh-based methods (like a phase field coupled to a Lattice–Boltzmann method<sup>7–9</sup>) to particle-based methods (like Smoothed Dissipative Particle dynamics<sup>10,11</sup>), to methods based on the use of the Green function or Dirac delta (like the boundary integral method<sup>12–14</sup> or immersed boundary method<sup>15</sup>). The practical implementation of some of those methods can be highly complex and computationally demanding. For instance, the Lattice–Boltzmann method simulates the Boltzmann equation to solve the fluid flow, which is highly complex to implement. Dissipative particle dynamics simulates a viscous fluid, however the viscosity has to be determined numerically which forces the algorithm to change *ad hoc* physical parameters to tune the conservative and dissipative forces, and physical scales can only be inferred indirectly.<sup>16</sup> Finally, smoothed dissipative particle dynamics solves some of these problems but some

constraints such as incompressibility can still be tricky to force and some fine-tuning needs to be in place to avoid spurious viscoelastic or shear-thinning behaviours.<sup>17</sup>

The phase-field methodology successfully models liquid–solid and liquid–liquid interfaces and, recently, it has also been used for modelling vesicles and simple cells like red blood cells.<sup>7–9,18–26</sup> The phase-field method reproduces accurately membrane morphology and dynamics under a flow in combination with the Lattice–Boltzmann method.<sup>7–9,26</sup> Previous work has focused on giving exhaustive phase diagrams of red blood cell morphologies both in 2D<sup>13,14</sup> and in 3D<sup>10,27</sup> where aside from deformation, other dynamics like *tumbling* are studied. The dimensionality of the study is also relevant, as a vesicle and a red blood cell are indistinguishable in 2D. In 3D the cytoskeleton made by a spectrin-network attached to a RBC membrane gives the membrane resistance to in-plane shear. This can be very important in some health disorders like hereditary spherocytosis.<sup>28,29</sup> Although the dimensional difference might not be important for the membrane shape under normal conditions, it can be of great importance for the results of some parameters or scalings. While lacking the in-plane shear can make it challenging to give quantitative results with 2D simulations, extensive previous qualitative research on healthy RBC in a microchannel has been proven successful. This is even more obvious when comparing with experimental results for different values of cytoskeleton elasticity for healthy cells<sup>30</sup> where the same shapes as in 2D simulations<sup>7</sup> are obtained.

Here, we present a methodology to simulate interfaces and, in particular, membranes coupled to a flow where the approach relies directly upon basic fluid mechanics equations. Consequently, we

<sup>a</sup> *Departament Física de la Matèria Condensada, Universitat de Barcelona, E-08028 Barcelona, Spain. E-mail: fdzgallen@gmail.com*
<sup>b</sup> *Instituto de Investigación Tecnológica (IIT), Universidad Pontificia Comillas, Madrid, E28015, Spain*
<sup>c</sup> *Institute of Nanoscience and Nanotechnology (IN2UB), 08028 Barcelona, Spain*

† Electronic supplementary information (ESI) available. See DOI: 10.1039/d1sm00559f

find this methodology ideal to add further extensions such as including more sophisticated constitutive equations (for instance, Maxwell or Oldroyd viscoelasticity) which is far from straightforward using, for example, Lattice–Boltzmann method.

In this work, we solve the equations for the vorticity and stream functions to avoid some subtleties of solving explicitly the Navier–Stokes equations. An additional benefit of this method is fulfilling the incompressibility condition regardless of the accuracy of the solving method. Our method is simpler and physical scales are explicit in the model, so it is a viable alternative to the Lattice–Boltzmann method, dissipative particle dynamics or smoothed dissipative particle dynamics. We illustrate our approach studying red blood cells in Poiseuille flow in two dimensions, immersed in either a narrow or a wide channel. In the case of a Poiseuille flow in a wide channel we show that the RBCs present short-lived metastable configurations that have not been previously observed in other studies. To prove the model presented here we also reproduce the so-called tumbling dynamics,<sup>14,27</sup> proving the versatility of our approach.

## 2 Methods

### 2.1 Description of the model

The model is based on the well-known Canham–Helfrich energy

$$F = \int_A \left( \frac{\kappa}{2} C^2 + \gamma_A \right) dA + \int_V \Delta p dV, \quad (1)$$

where  $C$  is the total curvature,<sup>31,32</sup> which has an associated energy scale, the bending modulus  $\kappa$ . In addition to the curvature term, the terms proportional to  $\gamma_A$  and  $\Delta p$  guarantee area and enclosed volume conservation, respectively.

We can rephrase the energy in eqn (1) – which has a purely geometrical interpretation – using a phase-field (also known as order parameter)  $\phi$ .<sup>18,19</sup> This order parameter describes the two phases: the extracellular ( $\phi = +1$ ) and the intracellular ( $\phi = -1$ ) phases. The membrane is the narrow region (of thickness  $\sim \varepsilon$ ) between both phases. The resulting expression for the energy is

$$F[\phi] = \int_V \left( \frac{\kappa}{2} [-\phi + \phi^3 - \varepsilon^2 \nabla^2 \phi]^2 + \gamma_1 \varepsilon^2 (\nabla \phi)^2 + \gamma_2 (1 - \phi^2)^2 + \beta \phi \right) dV, \quad (2)$$

where  $\gamma_i$  are two Lagrange multipliers to ensure area conservation and  $\beta$  is the Lagrange multiplier to ensure volume conservation, which will be discussed later. Note that the first term in eqn (2) captures the surface contribution in eqn (1) as it is almost zero except around  $\phi = 0$ .

With this formulation, we can write an equation for time evolution of the phase field as

$$\partial_t \phi(\vec{x}, t) = M \nabla^2 \mu, \quad \text{where } \mu = \frac{\delta F[\phi]}{\delta \phi} \quad (3)$$

where the chemical potential  $\mu$  is the functional derivative of the energy,<sup>33</sup>  $M$  is the mobility coefficient of the phase field and  $\partial_t$  denotes the partial derivative with respect of time. The

mobility  $M$  sets the time-scale of the phase-field interface formation and stabilization. We set this parameter to guarantee that the formation of the diffuse interface and its relaxation do not alter the simulation results. Quantitatively, the value of  $M$  is such that the membrane deformation time-scale  $\tau_\kappa = \eta l^3 / \kappa$  is  $10^5$  times slower than the phase field time-scale  $\tau_\phi = \varepsilon^2 / M$ . The explicit expression of the chemical potential for a Helfrich membrane is

$$\mu = \kappa((3\phi^2 - 1)\Phi[\phi] - \varepsilon^2 \nabla^2 \Phi[\phi]) - \gamma_A \nabla^2 \phi + \beta \phi, \quad (4)$$

where we define  $\Phi[\phi] = (-\phi + \phi^3 - \varepsilon^2 \nabla^2 \phi)$  to ease the formulation.

Eqn (3) minimizes the Canham–Helfrich energy in the absence of fluid, so we need to couple the latter equation with the velocity field. As the fluid transports the cell and the cell distorts the fluid, we have,

$$\partial_t \phi = M \nabla^2 \mu - \vec{v} \cdot \nabla \phi, \quad (5)$$

and

$$\rho(\partial_t \vec{v} + \vec{v} \cdot \nabla \vec{v}) = -\nabla P + \eta \nabla^2 \vec{v} - \phi \nabla \mu, \quad (6)$$

where  $\rho$  is the density,  $P$  is the pressure and  $\eta$  is the viscosity of the fluid. The term  $-\phi \nabla \mu$  accounts for the effect of the cell on the fluid. We should not forget that the hydrodynamics in 2D is noticeably different from 3D due to its even longer range. However, this is not a problem in our study because the behaviour of the Oseen tensor in our system is dominated by the characteristic finite size of our micro-channel.

To avoid some subtleties of other methods (like guaranteeing fluid incompressibility) we rephrase eqn (6) in terms of the vorticity and the stream functions, defined respectively as

$$\vec{\omega} = \nabla \times \vec{v}, \quad \nabla \times \vec{\xi} = \vec{v}. \quad (7)$$

The vectors vorticity  $\vec{\omega}$  and stream function  $\vec{\xi}$  have only one non-zero component thus we define  $\vec{\omega} = (0, 0, \omega)$  and  $\vec{\xi} = (0, 0, \xi)$  so, hereafter, we will work only with their unique non zero scalar component. Using these two variables, we find that the phase-field is coupled with two scalar Poisson equations

$$\partial_t \phi = M \nabla^2 \mu - (\partial_y \xi \partial_x \phi - \partial_x \xi \partial_y \phi), \quad (8)$$

$$\nabla^2 \omega = \frac{1}{\eta} (\partial_y \mu \partial_x \phi - \partial_x \mu \partial_y \phi), \quad (9)$$

$$\nabla^2 \xi = -\omega. \quad (10)$$

as, in 2D, the vorticity  $\omega$  and the stream function  $\xi$  have only one non-zero component.

For a Poiseuille flow, we translate the boundary conditions for the fluid into a set of equations for the vorticity and the

stream function using the unperturbed (without cell) solution:

$$v_x(y) = -\frac{dP}{dx} \frac{1}{2\eta} y(h-y) \Rightarrow \begin{cases} \xi(h) = \frac{dPh^3}{dx 6\eta} \\ \xi(0) = 0 \\ \omega(h) = -\frac{dPh}{dx \eta} \\ \omega(0) = \frac{dPh}{dx \eta} \end{cases}, \quad (11)$$

where  $h$  is the channel height and  $\frac{dP}{dx}$  is the pressure gradient.

As can be seen the code sample we share<sup>34</sup> we solve iteratively eqn (8)–(10): first we use a finite-difference scheme (space step  $\Delta x$ ) to solve the scalar Poisson equations that enter the dynamical eqn (8) that is solved using an explicit Euler discretization for the time step. We chose  $\Delta x$  to have enough resolution to describe the cell width (long semiaxis  $\sim 65\Delta x$ ) and the channel width (for width–cell ratios  $r$  from 1.5 to 6). This width–cell ratio  $r$  is comparing the size of the channel with the undeformed cell. We start all the simulations with an ellipsoid which has the reduced volume of a discocyte shape. This initial shape will evolve to a discocyte and will flow due to the interaction with the stream function field.

## 2.2 Physical constraints and Lagrange multipliers

As stated before, we have to ensure that the system conserves the area and the enclosed volume of the membrane. These are our physical constraints that we will ensure with the use of Lagrange multipliers. The enclosed volume can be computed with  $\int \phi(\mathbf{r}) dV$ , however for the area there are two different expressions

$$A_1 = \int \frac{3}{4\sqrt{2\varepsilon}} |\nabla\phi|^2 dV \text{ and } A_2 = \int \frac{3}{4\sqrt{2\varepsilon}} (1 - \phi^2)^2 dV,$$

and both are equal at the  $\varepsilon \rightarrow 0$  limit.

For simulations without a flow the area conservation can be ensured using the explicit Lagrange multiplier from ref. 35 with the addition of a velocity term for the expression  $A_1$

$$\gamma_1 = \frac{\int (-\nabla\phi \cdot \nabla(\mathbf{v} \cdot \nabla\phi) + M\nabla\phi \cdot \nabla\nabla^2\mu_0) dV}{M\int \nabla\phi \cdot \nabla\nabla^4\phi dV}. \quad (12)$$

This solution is obtained from the dynamic equation of the phase field, defining an unknown Lagrange multiplier for  $\nabla\phi$  and solving for it. This multiplier is enough to conserve the area for zero or low speed simulations but to explore the high velocity flows further precision was necessary.

Following Qiang Du, *et al.*<sup>21</sup> we have extended the Lagrange multiplier for the area and added one for the volume. This approach is accurate in the range of low to moderate velocities used in our work. As the first Lagrange multiplier is obtained for the first area expression we add a second Lagrange multiplier for the other expression and implement it with a simpler penalty approach. This second area multiplier does not need to be as accurate as the first as it just only gives additional support to the area conservation

$$\gamma_2 = C_\gamma(A(t) - A_0),$$

where  $C_\gamma$  is the weight given to this penalty for the area.

Finally a Lagrange multiplier for the volume conservation is also added with a penalty approach

$$\beta = C_\beta(V(t) - V_0),$$

where  $C_\beta$  is the weight given to this penalty.

## 3 Results

The code used to compute all the following results can be obtained from its GitHub repository.<sup>34</sup>

### 3.1 Poiseuille flow in a narrow channel

Poiseuille flow occurs when a constant pressure gradient is applied parallel to the channel walls. The cell travels with the flow and deforms due to the force exerted by the fluid. The total deformation changes continuously when the mean velocity in the channel increases adopting different shapes and orientations as shown in Fig. 1A–D.

In particular, Fig. 1 shows that, for narrow channels, increasing velocities change the shape of the cell from a discoid to an almost horizontal slipper (Fig. 1B). Also, larger velocities break the symmetry of the cell along its longest and shortest axes. Finally, for even larger velocities, the cell adopts the so-called *parachute* morphology, as shown in Fig. 1D. In this regime, the velocity field in the channel is the dominant mechanism of deformation.

These results prove that our phase-field formulation reproduces the morphologies observed experimentally and, also, those reported using alternative computational formulations. In particular, the results in ref. 7–9 in which a Helfrich model for the membrane was coupled with a Lattice–Boltzmann description of the flow.

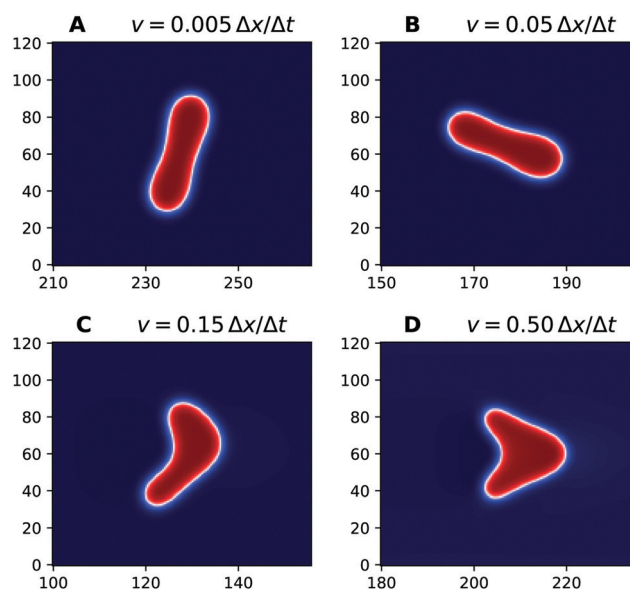
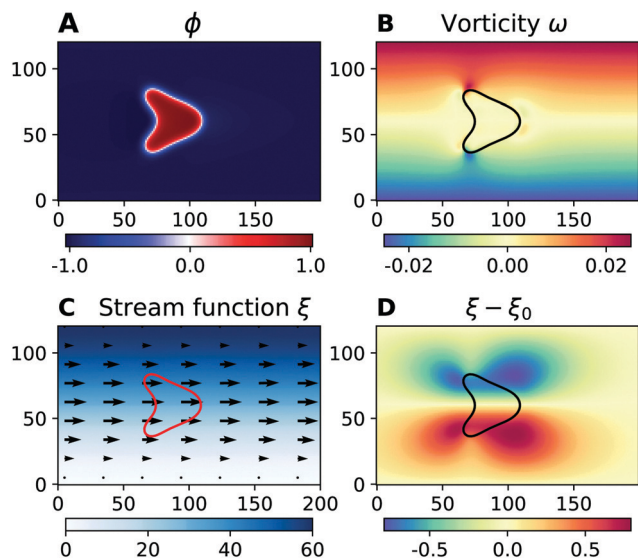


Fig. 1 Cell morphologies in confined channels. (A–D) Different flow speeds from slower to faster with a width–cell ratio of  $r = 1.5$ , 2 orders of magnitude from the fastest to the slowest.



**Fig. 2** Simulation of cell flow in a channel with width–cell ratio  $r = 1.8$ . (A) Parachute morphology; (B) vorticity; (C) stream function and velocity field being symmetrical with respect to the channel center, as the parachute also has a symmetric shape; and (D) deviations of the stream function with respect to an empty channel. Note how the stream function deviations are significant at distances comparable to the cell. Simulation of a channel  $400 \times 121\Delta x$  in size with a flow speed of  $0.5\Delta x/\Delta t$  and a viscosity of  $\eta = 1$ , and consisting of  $4 \times 10^7$  iterations.

Eqn (8)–(10) couple explicitly the vorticity and the stream function with the phase-field. In Fig. 2 we display those observables as well as the variation of the stream function due to the presence of the cell  $\xi - \xi_0$ , where  $\xi_0$  is the stream function in the absence of a cell. Far from the cell, the fluid field follows a parabolic shape (Fig. 2B) as expected for a Poiseuille flow. Apparently, the total stream function is quantitatively identical to the eye as the cell travels with the flow. However, the deviations of the stream function with respect to an empty channel highlight the relative motion of the fluid caused by the deformation of the membrane (Fig. 2D). Thus, while the cell affects the vorticity locally (near the membrane), the deviations of the stream function,  $\xi - \xi_0$ , display long range correlations: the fluid is perturbed at distances comparable to the size of the cell and the channel width.

Fig. 3A shows that the fluid is locally slowed down inside the cell and speeds up close to the tips of the *parachute*. On the other hand, the deviations of the vertical component of the velocity field explains the pattern of vorticity shown in Fig. 2.

But beyond the kinematics of the fluid, which mechanisms underlie the deformation and consequent effect of the cell over the fluid? To answer that question, we compute the local pressure field and the transverse component of the stress tensor,  $\sigma_{xy}$ , as summarized in Fig. 3.

The pressure field is obtained from the Gibbs–Duhem relation for constant temperature  $dP = \phi d\mu$ .<sup>7</sup> The patterns observed for  $v_x - v_{x0}$  in Fig. 3A can be explained by the pressure field. Thus, the cell is compressed along the center of the

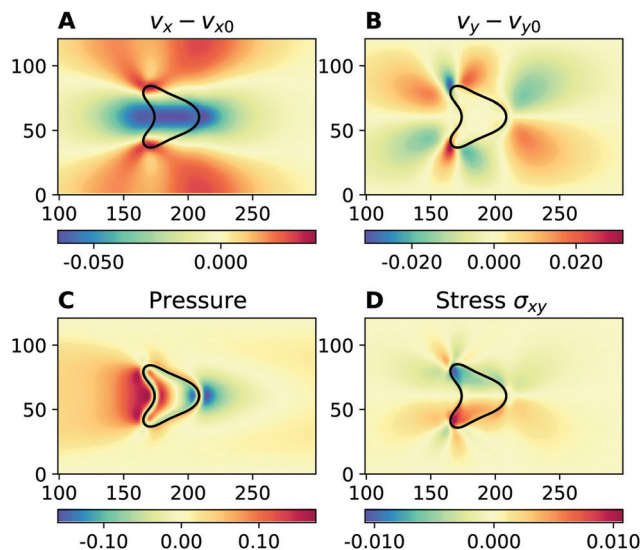


**Fig. 3** Symmetric parachutes. (A) Deviations of the horizontal velocity with respect to an empty channel; (B) deviations of the vertical velocity with respect to an empty channel; (C) fluid pressure; and (D) shear stress. Same simulation parameters as in Fig. 2.

channel due to excess pressure on the left and a local depression on the right. The shape of the cell remains symmetric and travels rigidly with the fluid, consistent with previous simulations.<sup>36</sup>

On the other hand, the shear stress,

$$\sigma_{ij} \equiv \nabla_i v_j - \nabla_j v_i, \quad (13)$$

makes the fluid cycle around the head and tips of the cell, as shown in Fig. 3D. The stress is maximum (in absolute value) at the cell tips dragging the fluid close to the tips (Fig. 3A) and increasing the vorticity by pushing the fluid vertically close to the tips (Fig. 3B). Inspection of the pressure and the stress emphasizes that regions with large pressure (in absolute value) correspond to lower shear stress.

The situation is slightly different for non-symmetric shapes as shown in Fig. 4. In this case a slipper travels with the fluid but, the cell center of mass is displaced towards one of the walls and the shape is no longer symmetric. As a consequence, at the front (right side) of the cell, both the pressure and the shear stress are large. This creates a non-trivial velocity pattern as shown in Fig. 4A and B and keeps the cell travelling rigidly instead of tumbling (rotating clockwise) as it travels. Thus, the cell is deformed just to keep the flow stationary.

As shown in Fig. 5, the deviations of the stream function  $\xi - \xi_0$  vary considerably far from the cell creating (relative) fluid re-circulation around the cell. The asymmetry of the cell is reflected in the shape of the stream lines. Also, inspection of the deviations of the vorticity with respect to an empty channel,  $\omega - \omega_0$ , show that the effect of the cell on the flow is focused on the areas with larger curvature as a consequence of the friction between the cell and the fluid.

To quantify this (global) interaction between the cell and the fluid, in Fig. 6 we show the square of the deviations – both of

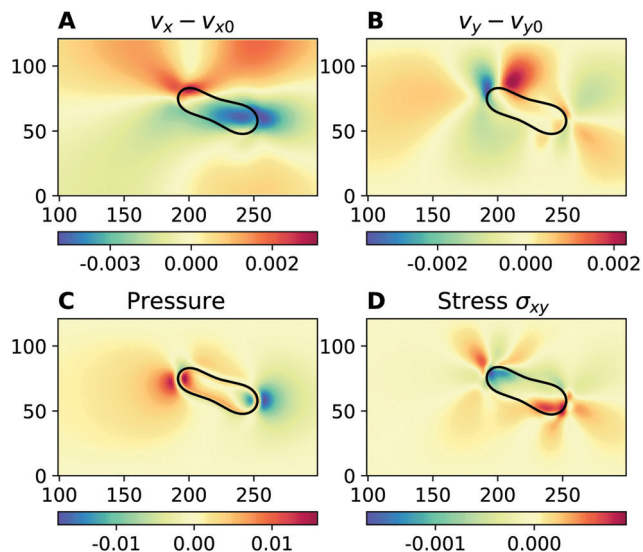


Fig. 4 Slippers. (A) Deviations in the horizontal velocity with respect to an empty channel; (B) deviations of the vertical velocity with respect to an empty channel; (C) fluid pressure; and (D) shear stress. Simulation of a channel  $400 \times 121\Delta x$  in size with a flow speed of  $0.05\Delta x/\Delta t$  and a viscosity of  $\eta = 1$ , and consisting of  $4 \times 10^7$  iterations.

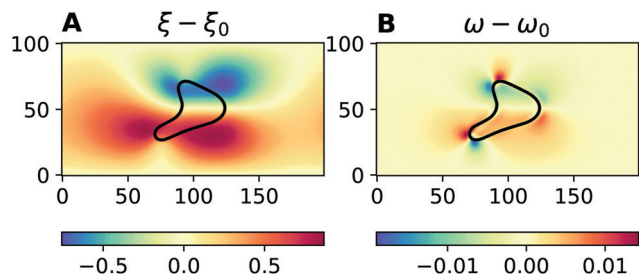


Fig. 5 Asymmetric parachutes. Cell-induced (A) stream function and (B) vorticity deviations with respect to an empty channel. Note how the stream function deviations are significant at distances comparable to the cell size. Flow speed  $v = 0.5\Delta x/\Delta t$  and size of channel  $200 \times 101$ .

the stream function and the vorticity – integrated throughout the channel

$$\mathcal{W} = \int_{\text{channel}} (\omega - \omega_0)^2 dV, \quad (14)$$

$$\mathcal{X} = \int_{\text{channel}} (\xi - \xi_0)^2 dV. \quad (15)$$

These observables allow us to track the deformation history of the cell. Actually, Wu<sup>37</sup> showed that the vorticity integrated throughout the channel is conserved in two-dimensional incompressible flows also in the presence of immersed solid bodies. Thus, we can use the integral of the deviations of the vorticity (14) as a measure of the elastic deformation of the cell and the dissipation caused by friction between the cell and the flow. We integrate the square as we are not interested in the sign of the deviation. As shown in Fig. 6, the cell deforms quickly at short times adopting a symmetric elongated shape

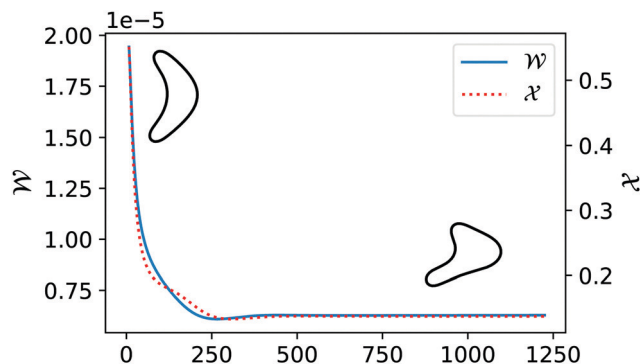


Fig. 6 Time evolution of the integrated squared cell-induced stream function  $\mathcal{X}$  and vorticity  $\mathcal{W}$  deviations with respect to an empty channel. These observables capture quantitatively the effect of the cell shape on the flow until the system reaches the steady state. Same simulation parameters as in Fig. 5.

that relaxes towards the final (non-symmetric) steady shape for long times.

### 3.2 Poiseuille flow in a wide channel: the transient *anti-parachute*

So far we have considered that the width of the channel is comparable to the size of the cell. In this section, we present results of studying channels whose width is several times larger than the size of the cell. The main difference is that, the larger the channel (for a fixed applied pressure gradient), the *flatter* the Poiseuille parabola. Thus, at the center of the channel we have a region of approximately constant speed and, consequently, lower shear stress. In these cases, the cell can evolve a shape we called the “*anti-parachute shape*”.

In Fig. 7A and B we show an example of a cell with an *anti-parachute shape* that becomes unstable and evolves into a slipper centered on the channel. We found that the *anti-parachute* is unstable for medium-width channels or for very wide channels at very high speeds.

It is worth noting that the shape of the *anti-parachute* has a different origin than the traditional parachute. In the case of the latter, the shape results from the increased velocities at the center of the channel so the cell adapts to the parabolic profile characteristic of the Poiseuille flow. However, for wide channels, the velocity gradient is not that large and the center of the channel is a region with an almost constant flow velocity. In that constant-speed region, the membrane does not follow the parabolic shape but results from the interaction between the membrane energy, the velocity and the shear stress. In this case, as the fluid circles around the cell it exerts a force on the membrane to reduce the drag. This force bends the cell in the opposite direction of a normal parachute shape resulting in the shape displayed in Fig. 7A.

The *anti-parachute shape* is more akin to what would happen to a surface tension interface rather than a bending one. In this case, the velocities at the cell edges are as high as the center of the channel. Thus, the bending contribution becomes subdominant with respect to the hydrodynamical

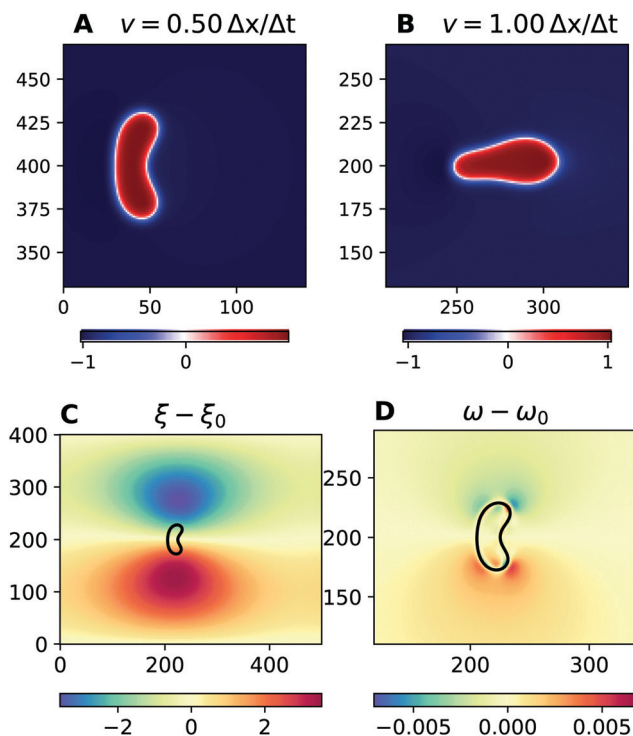


Fig. 7 Anti-parachutes. (A and B) Snapshot of a cell in a fast flow inside a wide channel. Cell-induced (C) stream function and (D) vorticity deviations with respect to an empty channel for a flow speed of  $v = 0.5\Delta x/\Delta t$ . Sizes of the channels: (A)  $600 \times 800$  and (B–D)  $500 \times 400$ . Width–cell ratios: (A)  $r = 12$  and (B–D)  $r = 6$ .

forces and the area conservation. In summary, the cell generates a resistance that is proportional to its cross-section, and the subsequent deformation is aimed to reduce the cell cross-section. As the flow speed is equal across the cross-section of the membrane, the cell simply bends in the flow direction instead.

Another quirk of this *anti*-parachute shape is that it is a metastable conformation of the cell that, eventually, rotates and deforms into a flow-oriented slipper. To quantify this transition, we compute the time course of the integrated squared vorticity deviation  $\mathcal{W}$  as in eqn (14). As shown in Fig. 8,  $\mathcal{W}$ , defined in eqn (14), presents two plateaus, which can be identified with each shape in Fig. 7A and B. Comparing the stability in Fig. 8 with the previous Fig. 6 we can clearly see two plateaus instead of one, where the first plateau corresponds to the *anti*-parachute shape. Following the result of ref. 37, we conclude that the *anti*-parachute morphology behaves as a solid object (conserved vorticity) during this transient time.

In the long term, the shape evolves into a slipper-shaped cell, but at the center of the channel. This result is also unexpected, as usually slippers have an equilibrium position outside the center of the channel.

The *anti*-parachute shape is symmetric with respect to the center of the channel most of the time. In contrast, if the initial location of the cell is far away from the center, the cell adopts a slipper shape early in the simulation and it travels towards the

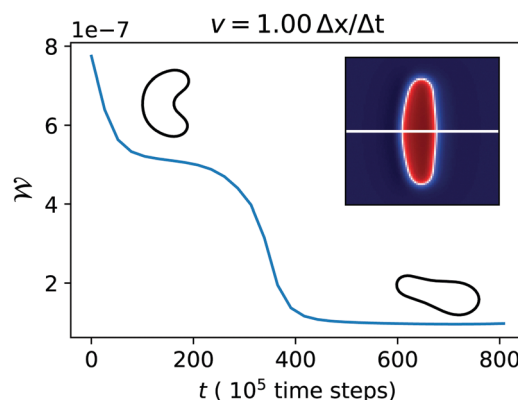


Fig. 8 Anti-parachutes. The sum of the squared deviation of the vorticity  $\omega$  and stream function  $\xi$  with respect to the expected value in the absence of a membrane. Inset of the initial conditions, shaped as an ellipsoid with the surface–volume ratio of a discocyte with a white line showing the center of the channel. The size of the channel is  $500 \times 400$ . We can see how each plateau refers to a given membrane shape. Width–cell ratios  $r = 12$ .

center, as shown in Fig. 9A. But, unlike the *anti*-parachute, Fig. 9B shows that the shape changes continuously and there is not any meta-stable morphology. Our results display some variability. On the one hand, the cell is close to the center but still tilted with respect to the center (which is likely to be a

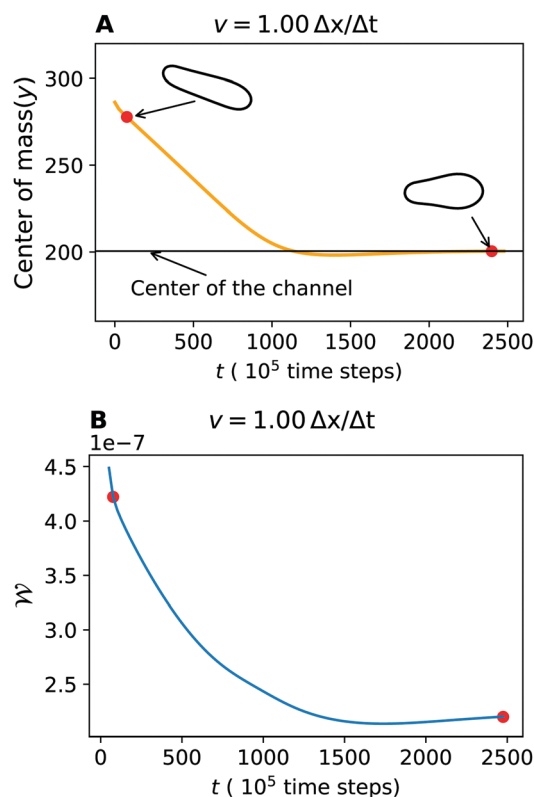


Fig. 9 Time evolution of the center of mass of a cell located initially displaced with respect to the center of the channel. The orientation as well as the location change continuously with time. The size of the channel is  $400 \times 400$ . Width–cell ratio  $r = 6$ .

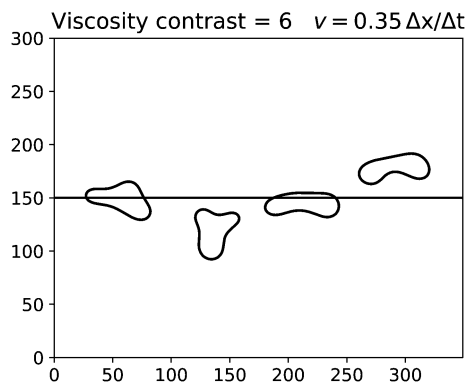


Fig. 10 Cell evolution over time; from left to right different snapshots are represented with advancing time. There is a black solid line indicating the center of the channel. Simulation of  $301 \times 350$  with a width–cell ratio  $r = 4.5$ .

metastable state). Also, simply due to the evolution of that particular simulation, finding the final equilibrium position takes much longer than the others.

So far, we have studied the case with a viscosity contrast equal to 1. In wider channels, this behaviour can be lost at high viscosity contrasts. In 2D simulations for high viscosity contrasts, the so-called tumbling dynamics are obtained.<sup>14,27</sup> In Fig. 10, we reproduce this sort of behaviour, proving the versatility of our approach. In this particular case, the initial location of the cell is slightly displaced above the center of the channel, so the symmetry is broken, and the tumbling mechanism can operate.

## 4 Conclusions

We have introduced a new mathematical formulation for two-dimensional deformable cells flowing in a channel. Our model is grounded in low-Reynolds fluid flow (Stokes equation) and, mathematically, combines the theory of phase-field models but captures accurately the deformations of a membrane in a laminar flow and the influence of the membrane on the fluid.

The simplicity of the model – one of its strengths – stems from the coupling of an equation for the membrane and an alternative description of the fluid based on integrating two Poisson equations for the stream function  $\zeta$  and the vorticity  $\omega$ . Another strength is that it fulfills the incompressibility condition regardless of the accuracy of the solving method thanks to its formulation.

Equipped with our model, we have replicated many existing results in the literature for red blood cells in low-Reynolds number flows such as the discocyte, the slipper, and the parachute in highly confined configurations (small cell-size to channel width ratios). These results prove the validity of the model. Besides this, for wide channels, we find a new metastable configuration: the *anti*-parachute. This transient behaviour might be relevant to understand the response of blood flow under sudden flow changes in the channel.

Using the connection between incompressibility and the conservation of the vorticity in the presence of rigid bodies, we can study the dynamics of the membrane deformation. We use the integrated value of the squared deviations of the vorticity with respect to an empty channel as a measure of the stability of the morphology until it reaches a steady state. When the *anti*-parachute loses its shape it becomes slipper-shaped, even at very high speeds but, unlike existing results in the literature, the slipper moves permanently to the center of the channel.

With this methodology we can also replicate known results for 2D cell simulations where tumbling is obtained at high viscosity contrast.<sup>14,27</sup> This further proves the capabilities of the method for different flow dynamics.

Our framework allows for the study of novel setups such as oscillating flows, channels with a varying cross-section, and extremely-confined flows, and will be the object of future studies.

## Conflicts of interest

There are no conflicts to declare.

## Acknowledgements

We acknowledge insightful discussions with I. Pagonabarraga. A. F. G. acknowledges financial support from MINECO (Spain) project FIS2016-78883-C2-1-P. This research has been funded by the Spanish Ministerio de Ciencia, Innovación y Universidades (MICINN)- Fondo Europeo de Desarrollo Regional funds of the European Union support, under Projects FIS2016-78883-C1-2-P/FIS2016-78883-C2-2-P and PID2019-106339GB-I00 (to M. C.). A. H. M. acknowledges financial support from Ministerio de Ciencia e Innovación (MICINN, Spain) project PID2019-1060636B-100.

## References

- 1 C. Minetti, V. Audemar, T. Podgorski and G. Couplier, *J. Fluid Mech.*, 2019, **864**, 408–448.
- 2 Z. Zhang, W. Chien, E. Henry, D. A. Fedosov and G. Gompper, *Phys. Rev. Fluids*, 2019, **4**, 024201.
- 3 S. H. Holm, Z. Zhang, J. P. Beech, G. Gompper, D. A. Fedosov and J. O. Tegenfeldt, *Phys. Rev. Appl.*, 2019, **12**, 014051.
- 4 G. Tomaiuolo, M. Simeone, V. Martinelli, B. Rotoli and S. Guido, *Soft Matter*, 2009, **5**, 3736–3740.
- 5 G. Tomaiuolo, M. Barra, V. Preziosi, A. Cassinese, B. Rotoli and S. Guido, *Lab Chip*, 2011, **11**, 449–454.
- 6 G. Tomaiuolo, L. Lanotte, R. D'Apolito, A. Cassinese and S. Guido, *Med. Eng. Phys.*, 2016, **38**, 11–16.
- 7 G. R. Lázaro, A. Hernández-Machado and I. Pagonabarraga, *Soft Matter*, 2014, **10**, 7195–7206.
- 8 G. R. Lázaro, A. Hernández-Machado and I. Pagonabarraga, *Soft Matter*, 2014, **10**, 7207–7217.

- 9 G. R. Lázaro, A. Hernández-Machado and I. Pagonabarraga, *Eur. Phys. J. E: Soft Matter Biol. Phys.*, 2019, **42**, 1–9.
- 10 J. Mauer, S. Mendez, L. Lanotte, F. Nicoud, M. Abkarian, G. Gompper and D. A. Fedosov, *Phys. Rev. Lett.*, 2018, **121**, 118103.
- 11 L. Lanotte, J. Mauer, S. Mendez, D. A. Fedosov, J.-M. Fromental, V. Claveria, F. Nicoud, G. Gompper and M. Abkarian, *Proc. Natl. Acad. Sci. U. S. A.*, 2016, **113**, 13289–13294.
- 12 O. Aouane, M. Thiébaud, A. Benyoussef, C. Wagner and C. Misbah, *Phys. Rev. E: Stat., Nonlinear, Soft Matter Phys.*, 2014, **90**, 033011.
- 13 N. Tahiri, T. Biben, H. Ez-Zahraouy, A. Benyoussef and C. Misbah, *Microvasc. Res.*, 2013, **85**, 40–45.
- 14 B. Kaoui, N. Tahiri, T. Biben, H. Ez-Zahraouy, A. Benyoussef, G. Biroš and C. Misbah, *Phys. Rev. E: Stat., Nonlinear, Soft Matter Phys.*, 2011, **84**, 041906.
- 15 C. D. Eggleton and A. S. Popel, *Phys. Fluids*, 1998, **10**, 1834–1845.
- 16 T. Ye, N. Phan-Thien and C. T. Lim, *J. Biomech.*, 2016, **49**, 2255–2266.
- 17 D. Alizadehrad and D. A. Fedosov, *J. Comput. Phys.*, 2018, **356**, 303–318.
- 18 F. Campelo and A. Hernandez-Machado, *Eur. Phys. J.: Spec. Top.*, 2006, **20**, 37–45.
- 19 F. Campelo and A. Hernández-Machado, *Phys. Rev. Lett.*, 2007, **99**, 088101.
- 20 F. Campelo and A. Hernández-Machado, *Phys. Rev. Lett.*, 2008, **100**, 158103.
- 21 Q. Du, C. Liu and X. Wang, *J. Comput. Phys.*, 2004, **198**, 450–468.
- 22 Q. Du, C. Liu and X. Wang, *J. Comput. Phys.*, 2006, **212**, 757–777.
- 23 X. Wang and Q. Du, *J. Math. Biol.*, 2008, **56**, 347–371.
- 24 T. Biben, K. Kassner and C. Misbah, *Phys. Rev. E: Stat., Nonlinear, Soft Matter Phys.*, 2005, **72**, 041921.
- 25 X. Yang and L. Ju, *Comput. Methods Appl. Mech. Eng.*, 2017, **315**, 691–712.
- 26 R. Chen, G. Ji, X. Yang and H. Zhang, *J. Comput. Phys.*, 2015, **302**, 509–523.
- 27 D. A. Fedosov, M. Peltomäki and G. Gompper, *Soft Matter*, 2014, **10**, 4258–4267.
- 28 S. Eber and S. E. Lux, *Semin. Hematol.*, 2004, 118–141.
- 29 X. An and N. Mohandas, *Br. J. Haematol.*, 2008, **141**, 367–375.
- 30 G. Tomaiuolo and S. Guido, *Microvasc. Res.*, 2011, **82**, 35–41.
- 31 P. B. Canham, *J. Theor. Biol.*, 1970, **26**, 61–81.
- 32 W. Helfrich, *Z. Naturforsch., C: J. Biosci.*, 1973, **28**, 693–703.
- 33 H. Goldstein, C. Poole and J. Safko, *Classical Mechanics*, 2002.
- 34 A. F. Gallen, MemPhaseFlow, 2021, <https://github.com/fdzgallen/MemPhaseFlow>.
- 35 C. Varea, R. Barrio and A. Hernandez-Machado, *Phys. Rev. E: Stat., Nonlinear, Soft Matter Phys.*, 2011, **84**, 061922.
- 36 T. Wang and Z. Xing, *BioMed Res. Int.*, 2018, **2018**, 8065252.
- 37 J. C. Wu, *AIAA J.*, 1981, **19**, 432–441.